



# Numerical Investigation of Broad Mid-Frequency Flexural Bandgap in Composite Sandwich Structures with Periodic Hollow-Shaped Core Geometry

Te-Han Chu<sup>1</sup> · Yu-Jui Liang<sup>1</sup>

Received: 26 December 2023 / Revised: 12 April 2024 / Accepted: 7 May 2024  
© Springer Nature Singapore Pte Ltd. 2024

## Abstract

**Objective** Periodic structures have been widely investigated in the past decade because of its potential for noise and vibration reduction. However, there is limited research applying the concept of periodic structures to composite sandwich structures. This paper proposes two lightweight types of periodic hollow-shaped cores in composite sandwich structures, which are simple geometries and able to generate wide flexural bandgap in mid-frequency range for broaden applications.

**Methodology** Floquet theory and wave finite element method are used to compute the bandgap behavior. The frequency response function (FRF) of the proposed structures is performed to demonstrate the performance of vibration attenuation by using the finite element simulation.

**Results and Conclusions** The FRF shows that the low vibration transmissibility is observed within a certain frequency range, which is consistent with the predicted flexural bandgap. The effect of face–core delamination on the FRF is also examined. Our findings indicate that the proposed structures have higher performance of vibration attenuation than the pristine conventional sandwich structures, even when the proposed structures exhibit face–core delamination. Last, our study demonstrates that despite the simplicity of the core design, it is capable of achieving comparable bandgap behavior to more complex geometries.

**Keywords** Composite Sandwich Structures · Vibration Attenuation · Bandgap · Finite Element Simulation

## Introduction

Vibration control and mitigation have become critical considerations in various engineering applications, ranging from aerospace and automotive applications to civil engineering and structural design. The ability to suppress and attenuate vibrations within specific frequency ranges is essential for ensuring structural integrity, user comfort, and overall performance in various systems and components. The filtering of vibrational waves, which is a difficult task, has attracted substantial interest as a means to enhance

the safety and quality of structures. Such filtering involves impeding the transmission of acoustic or elastic waves in certain frequency ranges, which is known as bandgap or stop-band behavior.

Many research in the past decades have been used to investigate the bandgap behavior of structures. Studies have recognized Bragg scattering and local resonance as the primary mechanisms underlying the production of bandgap behavior in periodic structures. Bragg scattering occurs when periodic impedance mismatches within a structure. When waves encounter such impedance variations periodically, the scattering is generated at the boundaries of the unit cell. The scattering can be caused by various factors, such as inclusions, geometric inconsistencies [1, 2], or material inhomogeneity [3–5]. When the interaction between reflected waves and incident waves results in destructive interference, wave propagation is hindered or completely stopped [6, 7], which results in the formation of a bandgap. However, generating wide low-frequency bandgaps through

---

✉ Yu-Jui Liang  
yliang@gs.ncku.edu.tw

Te-Han Chu  
p46111135@gs.ncku.edu.tw

<sup>1</sup> Department of Aeronautics and Astronautics, National Cheng Kung University, Tainan 701, Taiwan

Bragg scattering is challenging. The generation of low-frequency Bragg band gaps requires large lattice constant [8], which is difficult to achieve in practical applications.

Locally resonant band gaps occur when certain elements or substructures within the unit cell structure exhibit resonant behavior. To form a locally resonant band gap, a soft material is preferred as the matrix material, and a relatively hard and high-density material is embedded in or attached to the matrix material, e.g., phononic crystals [9–12]. Numerous researchers have used a spring–mass system directly connected to a beam or plate-type structure to generate a low-frequency bandgap [13, 14]. In contrast to bandgaps generated through Bragg scattering, bandgaps generated through local resonance are not strongly influenced by the size of the unit cell and can be achieved at low frequencies with unit cells that are considerably smaller than the corresponding wavelengths. Therefore, the locally resonant mechanism has attracted extensive attention in recent years and some studies have even coupled the aforementioned two mechanisms for bandgap generation. For example, Chen et al. [15] proposed a composite beam with an interleaved core and resonator. They theoretically and experimentally investigated the beam and found that it can generate a low-frequency bandgap at 500 Hz. Although locally resonant mechanism generate low-frequency bandgap easier, the result of total structure becomes heavier.

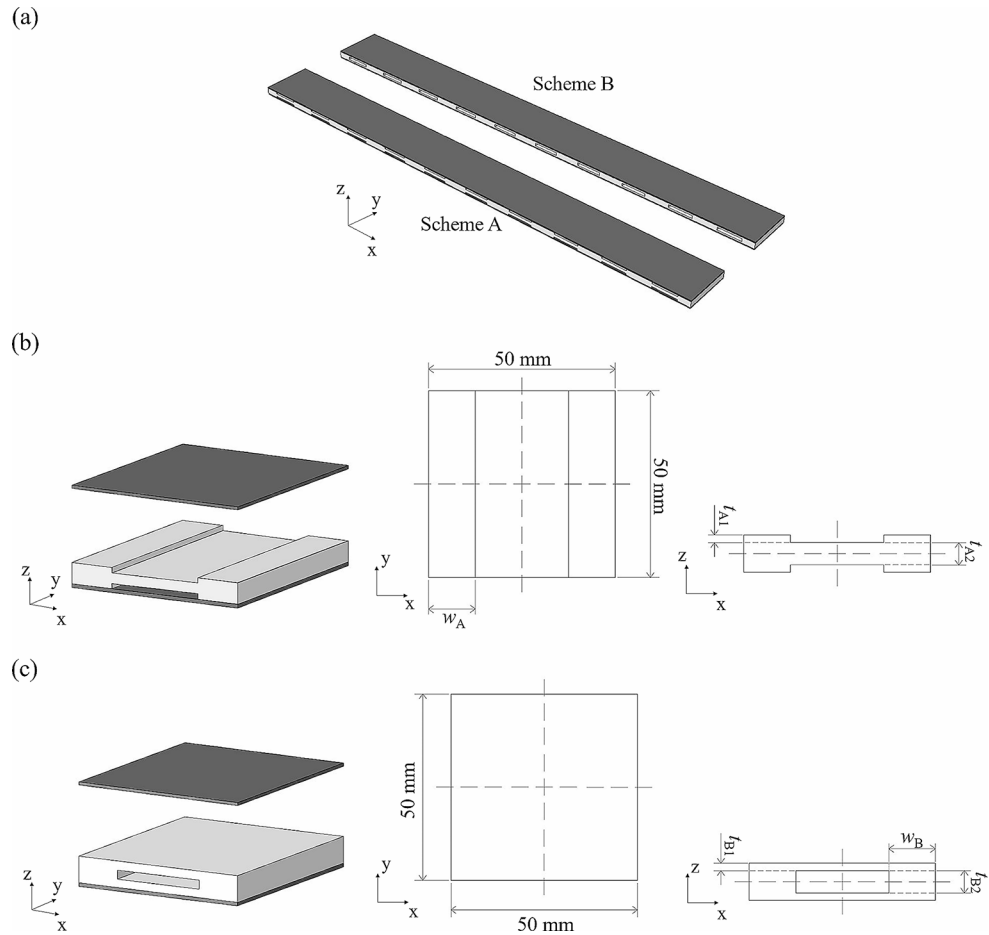
In certain situations, such as abrupt changes in natural environmental conditions or disturbances caused by human activities, external vibrations exhibit considerable variations. Consequently, the design of wide-bandgap structures is receiving increasing attention. Several studies have achieved bandgaps with a wide frequency range. Domadiya et al. [16] achieved an ultrawide bandgap (bandwidth approximately 2000 Hz) in the middle-frequency range for a phononic beam with cross-sectional variations in material properties; the experimental results agreed well with the theoretical results. A few studies have attempted to optimize structures with wide and low-frequency bandgaps. For example, Chronopoulos et al. [1] proposed an optimization method to enhance the bandgap width and lower the center frequency of bandgap. Jeon et al. [17] developed a tapered beam with an ultrawide and ultralow-frequency bandgap (below 100 Hz) and investigated the effect of geometric parameters on the bandgap behavior. Acar et al. [18] proposed a complex structure with a bandgap generated through inertia amplification and achieved a low-frequency bandgap near 300 Hz. In a later study, the shape of a phononic bandgap structure is optimized by incorporating the inertial amplification mechanism to broaden the bandgap [19].

Over the past five decades, composite materials and structures have been extensively developed and widely

utilized in industries such as the shipbuilding, automotive, and aerospace industries. Significant progress has been achieved in various types of composites including the state-of-the-art research, such as damage modeling methods [20, 21] and manufacturing techniques for laminated composites [22, 23]. One of the commonly used composite structure called composite sandwich structures comprises two thin but strong face sheets bonded to a core material. The core is often made of lightweight material, such as honeycomb panels or polymers, whereas the face sheets are made from strong and stiff materials, such as carbon-fiber-reinforced polymer [24]. Due to their lightweight and high stiffness properties, composite sandwich structures have emerged as a popular choice for mitigating vibration and effectively filtering vibration waves in practical applications. Ampatzidis et al. [25] proposed two composite sandwich beams with simple core geometries. These beams contain metamaterial cores, and the bandgaps were located in the middle-frequency range. The aforementioned beams are easy to manufacture and can thus be applied across a wide variety of domains.

Although many studies have developed different types of periodic structures, factors such as the complex geometries, manufacturing difficulties, and high-frequency bandgaps of these structures have restricted their practical applications. Therefore, inspired by several previous studies several [16, 17, 25], two types of composite sandwich structures are proposed in this paper. The objective of the present work is to design the composite sandwich structures with simple core geometries that still can have wide flexural bandgaps in intermediate-to-low-frequency ranges. In this paper, the unit cell of two proposed structures with detailed design and geometric dimensions are discussed first followed by the brief introduction of the analysis method and the bandgap behavior. Parametric studies of the flexural bandgap are discussed next to investigate the influence of changing geometric dimensions. The frequency response function (FRF) by using FE simulations is then performed to examine the flexural bandgap behavior and discuss the effect on different lengths of the proposed structures. Moreover, many references indicate that the delamination damage reduces the bending stiffness of sandwich structures and causes its natural frequency to occur in an undesirably low range [26]–[27]. Therefore, the effects of delamination on the FRF and the flexural bandgap behavior are investigated last.

**Fig. 1** (a) Schematics of the proposed structures with detailed dimensions of (b) scheme A and (c) scheme B



## Design and Analysis

### Structural Design

To expand the practical utility of composite sandwich structures, it is essential to carefully consider both the manufacturing process and the overall structural weight. Several innovative structural designs including intricate geometries and combination of different materials were demonstrated to achieve the wide bandgap behavior. However, employing multiple materials often necessitates secure bonding during fabrication, leading to increased complexity and the potential for debonding due to a higher number of bonding interfaces. Intricate geometries make challenges in achieving practical feasibility, further complicating their implementation. Also, structural weight is often sacrificed to achieve it to create the wide bandgap behavior in structures such as phononic crystals, or the combined materials by soft and stiff materials. Furthermore, limited research focus on the bandgap behavior in traditional composite sandwich structures. Therefore considering the aforementioned factors, two lightweight types of periodic hollow-shaped cores are proposed and applied to the composite sandwich structures

**Table 1** Material properties for numerical simulation [25]

Facesheet		Core
$E_x = 55 \text{ GPa}$	$G_{xy} = 1.2 \text{ GPa}$	$E = 75 \text{ MPa}$
$E_y = 50 \text{ GPa}$	$G_{yz} = 1.2 \text{ GPa}$	$G = 27.75 \text{ MPa}$
$E_z = 20 \text{ GPa}$	$G_{xz} = 3.6 \text{ GPa}$	$\rho = 100 \text{ kg/m}^3$
$\nu_{xy} = 0.4$	$\rho = 1420 \text{ kg/m}^3$	
$\nu_{yz} = 0.4$		
$\nu_{xz} = 0.25$		

as shown in Fig. 1(a). Both structures consist of two rectangular face sheets and a core, which are made of the carbon fiber reinforced polymers (CFRP) and PVC foam, respectively. The properties of the adopted materials are used as listed in Table 1 [25]. Figure 1(b) shows two different designs of the unit cells, namely schemes A and B in this paper. Comparing with the core geometry in conventional sandwich composites, two additional cut-outs on the top and bottom of the core are applied in scheme A, while a rectangular cut-out in the middle of the core is applied in scheme B. It can be seen that these two geometries are relatively simple, which enhances their practical applicability. The geometric dimensions of the irregular cores in schemes A and B are shown in Fig. 1(c) and Fig. 1(d), respectively. The geometries of both schemes are symmetric with respect to

the  $x$ -axis,  $y$ -axis, and  $z$ -axis. The length and width of both unit cells are all 50 mm, and the thickness of the CFRP face sheets is 1 mm. The total thickness of the core is initially set as 6 mm with  $w_A = w_B = 12.5$  mm,  $t_{A1} = t_{B1} = 1.5$  mm, and  $t_{A2} = t_{B2} = 3$  mm. Parametric studies of the core dimensions are discussed later in Sect. 3.

### Dispersion Curve and Bandgap Analysis

The wave finite element methodology [28–30] was used to calculate the bandgaps of the two proposed unit cells as briefly described in the following, and the first bandgap is mainly focused on this study. Both unit cells are arrayed periodically along the  $x$ -axis, which can be assumed as a one-dimensional problem. The kinematic motion of any node in a unit cell can be expressed as a time-harmonic vibration as follows:

$$\mathbf{q}(t) = \mathbf{q}e^{i\omega t} \tag{1}$$

where  $t$  is time and  $\omega$  is the harmonic wave frequency. The degrees of freedom of a unit cell are defined using the vector  $\mathbf{q}$  (Eq. 2). This vector can be divided into three components, namely  $\mathbf{q}_L$ ,  $\mathbf{q}_I$ , and  $\mathbf{q}_R$ , which correspond to the degrees of freedom on the left side, in the interior, and on the right side of the unit cell, respectively.

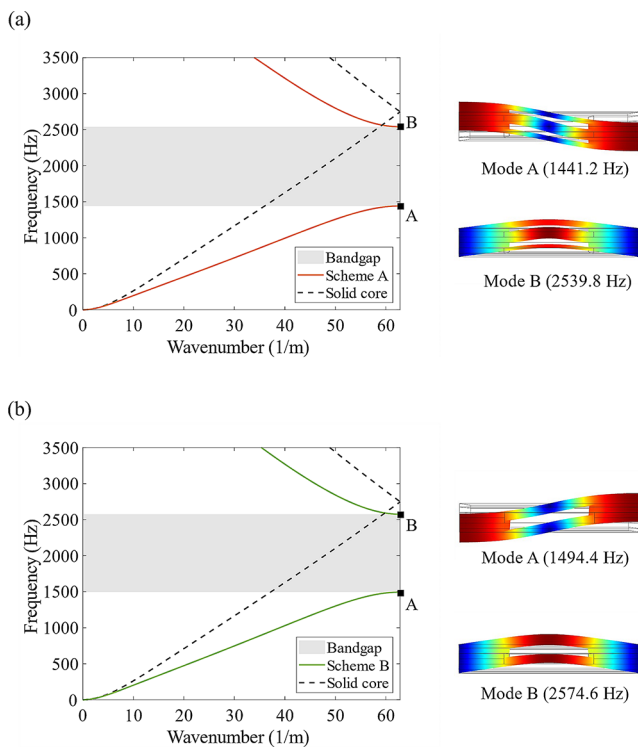


**Fig. 2** Dispersion curves and flexural bandgaps of (a) schemes A and (b) scheme B compared with the conventional composite sandwich with solid core. Mode A and B depict the vibration modes at the lower and upper bounds of the bandgaps in schemes A and B

$$\mathbf{q} = \begin{Bmatrix} \mathbf{q}_L \\ \mathbf{q}_I \\ \mathbf{q}_R \end{Bmatrix} \tag{2}$$

A Floquet periodic boundary condition is applied to the unit cell to determine the dispersion curve. Thus, the relation between the kinematics of the left and right nodes of the unit cell is expressed as follows:

$$\mathbf{q}_R = \mathbf{q}_L e^{-i\mu_x} \tag{3}$$

where  $\mu_x = k_x L_x$  is the propagation constant in the  $x$ -direction,  $k_x$  is the wavenumber, and  $L_x$  is the length of the unit cell in the  $x$ -direction. The equation of motion of a free vibration unit cell can be written as

$$(\mathbf{K} - \omega^2 \mathbf{M}) \mathbf{q} = 0 \tag{4}$$

Substituting Floquet periodic boundary condition into Eq. (4) and solve the eigenvalue problem, then the dispersion relation of proposed structures can be obtained. In this work, the COMSOL Multiphysics finite element software is used to compute the dispersion curve and bandgap of the proposed structures based on the Floquet theory and wave FEM. To analyze the flexural bandgap behavior, the displacement in  $y$ -direction of the entire unit cell is fixed in order to filter out in-plane shear wave and torsional wave. Next, the displacement in  $x$ -direction of neutral axis is fixed for filtering out longitudinal wave [17]. Floquet periodic boundary condition was applied to the left- and right side (along  $x$ -direction) of the unit cell and then flexural band behavior of the infinite periodic structures can be calculated. The reader is referred to the references [28–30] for more details.

Sweeping the wavenumber from point X to point  $\Gamma$  in the first Brillouin zone, the dispersive curve can be obtained. Figure 2 shows the dispersive relations of the schemes A and B, respectively. The core geometric dimensions are  $t_{A1} = t_{B1} = 1.5$  mm,  $t_{A2} = t_{B2} = 3$  mm, and  $w_A = w_B = 12.5$  mm in this case. The first flexural bandgap of the scheme A is computed between 1441.2 and 2539.8 Hz, while the first flexural bandgap of the scheme B is existed between 1494.4 and 2574.6 Hz. The dispersion curves of the solid core in conventional sandwich composites are also illustrated in Fig. 2 as comparisons, which indicates that no bandgap behavior is observed in the conventional sandwich structures.

Moreover, Fig. 2 depicts the vibration modes at the lower and upper bounds of the bandgaps in schemes A and B. Cheng et al. [31] proposed an analytical method for examining the effects of beam size and Poisson’s ratio on the bending stiffness and bandgap frequency of a micro-beam. The analytical result shows that the size effect increases

the bending stiffness of the micro-beam, causing the band gap to move to a higher frequency. Moreover, an increase in Poisson’s ratio led to a decrease in bending stiffness and bandgap frequency. Hans et al. [2] examined a diamond-like hole meta-plate and found that the lower and upper bound frequencies of the bandgap are depended on the vibration modes of the unit cell. In Fig. 2(a), it is observed that the mode A (1441.2 Hz) in scheme A is attributed to the shear motion, whereas the mode B (2539.8 Hz) is attributed to the symmetric bending motion. Similar observations are obtained in scheme B. In Fig. 2(b), the mode A (1494.4 Hz) at the lower-bound of the bandgap shows the shear motion. It can be seen that the mode A in scheme B is the direct converse of the mode A in scheme A. The mode B (2574.6 Hz) at the upper-bound of the bandgap corresponds to a symmetric bending mode.

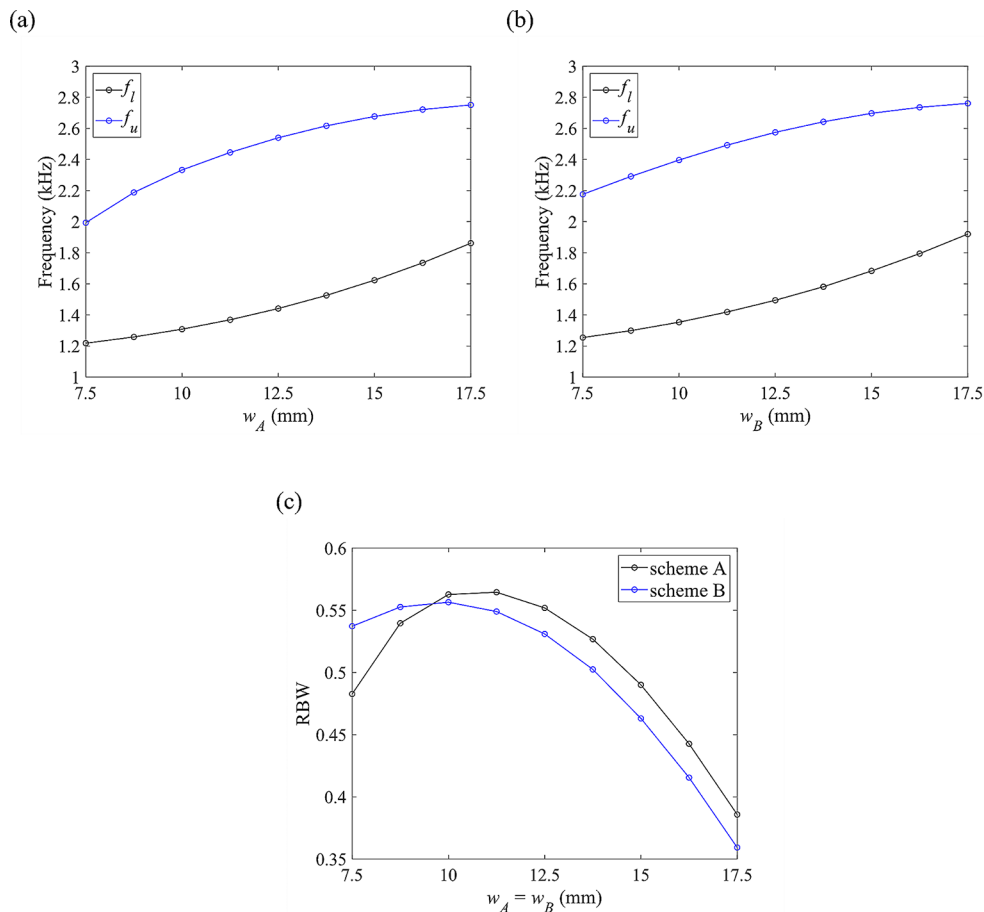
Although two different proposed schemes have similar bandgap behavior when the core geometric dimensions are initially set to  $t_{A1} = t_{B1} = 1.5$  mm,  $t_{A2} = t_{B2} = 3$  mm, and  $w_A = w_B = 12.5$  mm, the changes in the core geometry lead to different influence on their bandgap behaviors. Therefore, the parametric studies of the core geometry are investigated and discussed in the next section.

## Parametric Studies

### Effect of the Core Width

In this subsection, the influence of changing core width  $w_A$ ,  $w_B$  on the bandwidth and frequency range of the bandgap are discussed for both schemes A and B. To investigate the effect of different core width, the dimensions of the CFRP face sheets are remained at  $50 \times 50 \times 1$  mm<sup>3</sup> while other core geometric parameters  $t_{A1}$ ,  $t_{A2}$ ,  $t_{B1}$ , and  $t_{B2}$  are fixed the values of 1.5 mm, 3 mm, 1.5 mm, and 3 mm, respectively. Figure 3 depicts the fluctuations in the lower-bound frequency  $f_l$  and upper-bound frequency  $f_u$  of the bandgaps for schemes A and B with respect to variations in  $w_A$  and  $w_B$ , respectively (from 7.5 mm to 17.5 mm in intervals of 1.25 mm). As illustrated in Fig. 3(a), the  $f_l$  value gradually increases when  $w_A$  increases because the length of suspended portion in the middle of the core in scheme A is short, which causes shear stiffening with an increase in  $f_l$ . It can be explained that the vibration mode at the lower-bound frequency is attributed to the shear motion as shown at mode A in Fig. 2(a). If a low  $f_l$  value is desired,  $w_A$  needs to be decrease for a longer length of suspended portion in the middle of the core, and this causes shear softening and leads to a decrease in

**Fig. 3** Lower and upper bounds of the flexural bandgaps for (a) schemes A, (b) scheme B, and their (c) RBW with respect to the core width ( $w_A$ ,  $w_B$ )





$f_l$ . The lowest and highest  $f_l$  values for scheme A, namely 1218.1 Hz and 1861.3 Hz, are obtained under  $w_A$  values of 7.5 mm and 17.5 mm, respectively. Considering the feasibility of manufacturing, the value of  $w_A$  should not too small. Otherwise, the bonding area between the face sheets and the core becomes excessively small, which increases the possibility of delamination damage. On the other hand, the  $f_u$  value also increases with an increase of  $w_A$  because the vibration mode at the upper-bound frequency is attributed to the bending motion as shown at mode B in Fig. 2(a). A large value of  $w_A$  increases the bending stiffness of the unit cell and an increase in  $f_u$ , while a small value of  $w_A$  decreases the bending stiffness of the unit cell and a decrease in  $f_u$ . The lowest and highest  $f_u$  values for scheme A, namely 1993.2 Hz and 2751 Hz, are computed at  $w_A$  values of 7.5 mm and 17.5 mm, respectively. Figure 3(b) shows the variations in  $f_l$  and  $f_u$  with the core width  $w_B$  for scheme B. It can be seen that the  $f_l$  and  $f_u$  values of scheme B could be altered in the same manner as those of scheme A because of the identical vibration mode as shown in Fig. 2(b). For the width  $w_B$  varying from 7.5 mm to 17.5 mm, the lowest and highest  $f_l$  values for scheme B, namely 1254.5 Hz and 1920.2 Hz, and the lowest and highest  $f_u$  values namely 2175.9 Hz and 2761 Hz, are obtained under  $w_B$  values of 7.5 mm and 17.5 mm, respectively.

Figure 3(c) illustrates the variations in the relative bandwidths (RBWs) of schemes A and B with  $w_A$  and  $w_B$ , respectively. The RBW is defined as follows [32]:

$$\text{RBW} = \frac{f_u - f_l}{(f_u + f_l)/2} \quad (5)$$

where  $(f_u + f_l)/2$  represents the center frequency of the bandgap. As mentioned earlier, the increase of core width causes the increase of bending and shear stiffness of the unit cell. The value of RBW for scheme A is initially climbed from  $w_A$  value of 7.5 mm to 11.25 mm. Within this range, the elevation in shear stiffness exhibits a lesser effect compared to the increment in bending stiffness, and the observed increase is attributed to the RBW. As  $w_A$  is increased from 11.25 mm to 17.5 mm, the influence of shear stiffness is greater than the bending stiffness. It can be observed in Fig. 3(a) that the slope of  $f_l$  curve is enhanced rapidly while the slope of  $f_u$  curve is reduced, and the RBW then decreases rapidly in the  $w_A$  range of 11.25 mm to 17.5 mm. Similar behavior of RBW for scheme B is observed compared to the scheme A. When  $w_B$  is increased from 7.5 mm to 10 mm, the RBW is increased. When  $w_B$  is increased from 10 mm to 17.5 mm, the RBW is decreased. Noted that the RBW for scheme B is higher than that of scheme A when the core widths are 7.5 mm and 8.75 mm. On the contrary, the RBW for scheme A is higher than that of scheme B when

the core width is between 10 mm and 17.5 mm. Overall, the scheme A outperforms the scheme B in terms of the RBW. The highest RBWs for schemes A and B, namely 0.564 and 0.556, are achieved at core widths of 11.25 mm and 10 mm, respectively.

### Effect of the Core Thickness

The effect of the core thickness ( $t_{A1}$ ,  $t_{A2}$ ,  $t_{B1}$ , and  $t_{B2}$ ) on the bandgap are investigated in this subsection. The core widths  $w_A$  and  $w_B$  are fixed at 12.5 mm. The thickness ratios for scheme A ( $t_{A2}/t_{A1}$ ) and scheme B ( $t_{B2}/t_{B1}$ ) are kept constant at 2. The core thickness  $t_{A1}$  and  $t_{B1}$  are varied from 0.5 mm to 2.5 mm in intervals 0.25 mm each, while the  $t_{A2}$  and  $t_{B2}$  are correspondingly varied from 1 mm to 5 mm. Figure 4 illustrates the relationship between the lower-bound  $f_l$ , upper-bound  $f_u$  frequencies of the bandgaps and the core thickness as well as the RBWs for schemes A and B. As shown in Fig. 4(a) and (b), the values of lower-bound frequency  $f_l$  in the first bandgap for both schemes are increased slowly, which indicates the less effect of the shear motion in the unit cell when the core thickness is increased. On the other hand, the values of upper-bound frequency  $f_u$  in the first bandgap for both schemes are increased rapidly, which means the strong effect of the bending motion in the unit cell when the core thickness is increased. Although the first bandwidth in scheme A exists a sudden drop when core thickness  $t_{A1}$  is decreased from 1 mm, 0.75 mm to 0.5 mm, one distinction observed is that the second bandgap (dashed line) appears only in scheme A within that range and a new pass band appears that divides the single bandgap into two bandgaps as shown in Fig. 5. The mode A for three cases in Fig. 5 are all attributed to the shear motion which behave the same with the mode A displayed in Fig. 2. However, the mode B in Fig. 5(a) is not just a purely symmetric bending motion as discussed at mode B in Fig. 2. It represents a hybrid bending mode that involves the coupling of the symmetric bending motion of the entire unit cell with the resonant motion in the suspended portion of the unit cell. As the core thickness decreased, the suspended portion in the middle of the core is getting thinner to become softer. The flat second pass band is then observed and the locally resonant phenomenon becomes more clear as shown in modes C and D in Fig. 5(a) as well as the modes B, C in Fig. 5(b) and (c). The formation of the first bandgap becomes Bragg scattering coupling with locally resonant mechanism. Moreover, the bandwidth of the first bandgap is decreased while the bandwidth of the second bandgap is increased and moving down. This result can be attributed to the fact that when the thickness of the suspended portion  $t_{A2}$  is reduced, the bending stiffness itself is decreased, which leads to a decrease in the resonant frequency.

**Fig. 4** Lower and upper bounds of the flexural bandgaps for (a) schemes A, (b) scheme B, and their (c) RBW with respect to the core thickness ( $t_{A1}$ ,  $t_{B1}$ )

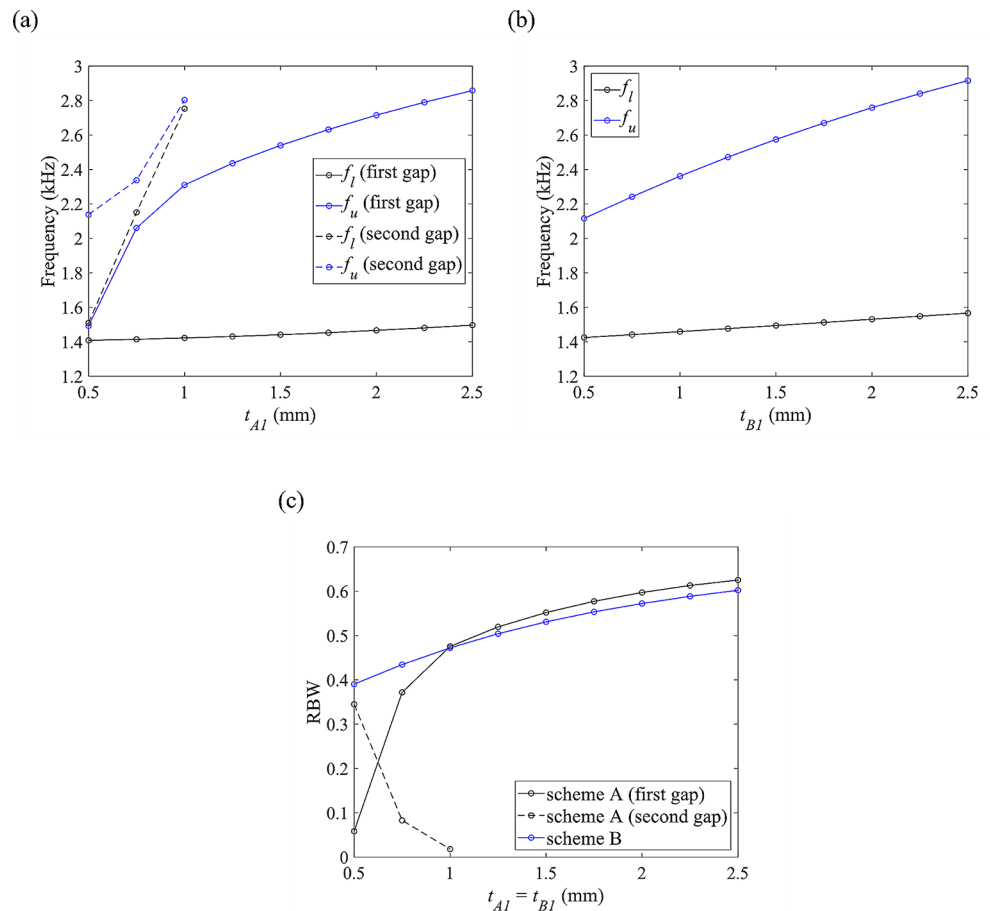


Figure 4(c) displays the RBWs of the bandgaps for both schemes. The RBWs in the first bandgap are increased for the entire range of  $t_{A1}$  and  $t_{B1}$ , which are different from the effect of core width on the RBW as discussed in previous section. The largest and smallest values of RBW in the first bandgap for scheme A and B are from 0.058 to 0.625 and from 0.390 to 0.602, respectively. As mentioned earlier, the second bandgap appears only in the scheme A due to the resonant motion of the suspended portion in the middle of the core. As the  $t_{A1}$  is within the range between 0.5 mm and 1 mm, the RBW values in the second bandgap are existed from 0.345 to 0.018. It indicates that more strong resonant effect is contributed to the second bandgap when the thickness of suspended portion is decreasing. As the core thickness is further increased from the  $t_{A1}$  value of 1 mm to 2.5 mm, the RBW of scheme A become slightly larger than that of scheme B. The RBWs of both schemes continue to increase with the core thickness without exhibiting any inflection point. This result is different from that observed for the effect of the core width ( $w_A$ ,  $w_B$ ) on the RBW. Overall, if a low-frequency bandgap is desired, the core width can be decreased to effectively reduce the lower-bound frequency of the bandgap. To obtain the larger possible RBW for first bandgap, a large core thickness can be selected to

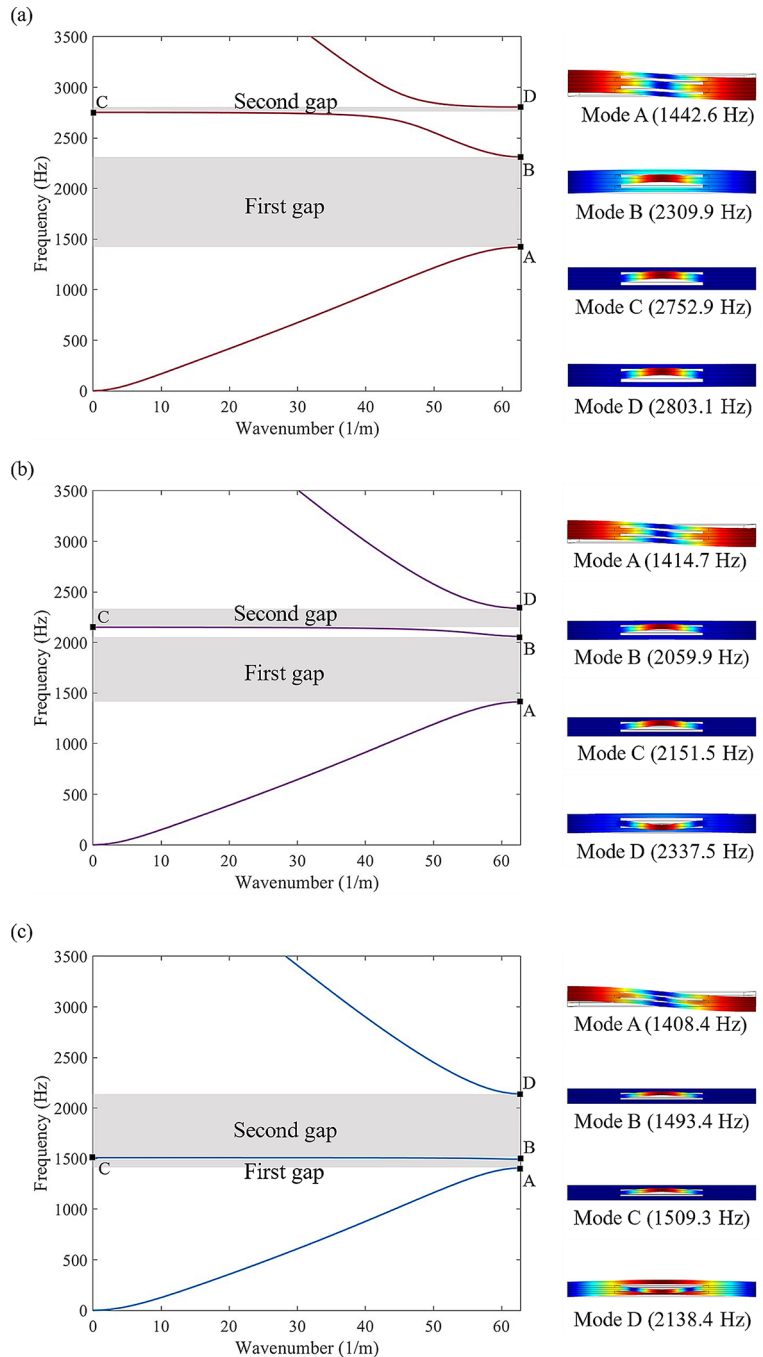
obtain a large RBW. Thus, increasing the core thickness does not increase the lower-bound frequency significantly but effectively increases the upper-bound frequency and the mechanical performance of the structure.

## Performance of Vibration Attenuation

### Numerical Models

The commercial FE software Abaqus is used to compute the frequency response function (FRF) for verifying the calculated bandgap behavior for schemes A and B. Figure 6 depicts the schematics of the finite element model for schemes A and B. The geometric parameters of the cores in schemes A and B are set as follows:  $w_A = 12.5$  mm,  $t_{A1} = 1.5$  mm, and  $t_{A2} = 3$  mm for scheme A;  $w_B = 12.5$  mm,  $t_{B1} = 1.5$  mm, and  $t_{B2} = 3$  mm for scheme B as discussed earlier in Sect. 2.2. The material properties [25] listed in Table 1 are assigned to the composite face sheet and the core. The C3D8 element type, which is an eight-node hexahedral solid element in three-dimensional, is adopted in the FE model. The unit cell of scheme A comprises 512 elements for the face sheets and 1024 elements for the core. The unit cell of

**Fig. 5** Dispersion curves, bandgaps, and different vibration modes in scheme A for different core thickness (a)  $t_{AI} = 1$  mm, (b)  $t_{AI} = 0.75$  mm, and (c)  $t_{AI} = 0.5$  mm



scheme B comprises 512 elements for the face sheets and 896 elements for the core. The interfaces between the face sheet and the core are subjected to tie constraints. To compute the FRF, an excitation force is applied at the left edge of the bottom face sheet, and the displacement response is measured at the right edge of the top face sheet (7).

### Effect of the Number of Unit Cells on the FRF

Previous research on the bandgap behavior of periodic structures has indicated that the influence of the number of unit cells on transmissibility of structures has to be considered. Jensen [33] analytically demonstrated that the extent of vibration attenuation depends on the number of unit cells. Studies [1, 16] have experimentally and numerically indicated that the bandgap behavior becomes more noticeable as more unit cells are present. To verify the effects of the



**Fig. 6** Schematics of the finite element model for schemes A and B (used for calculating FRF)

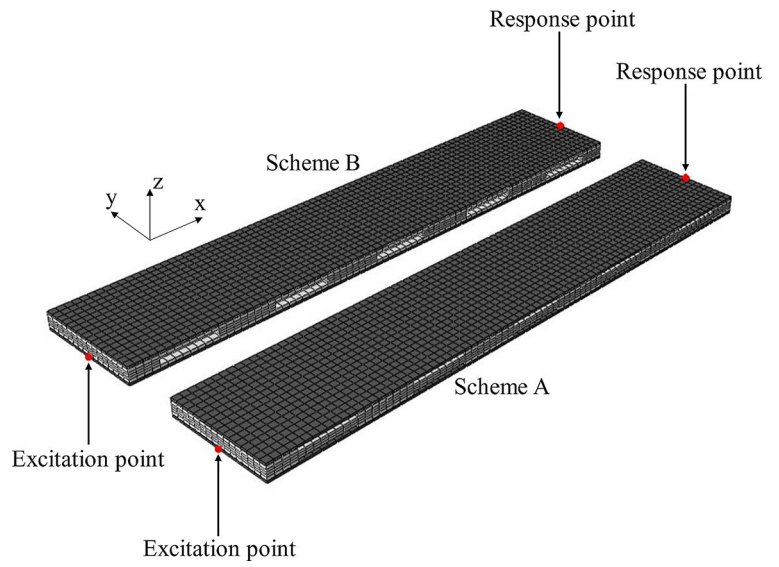
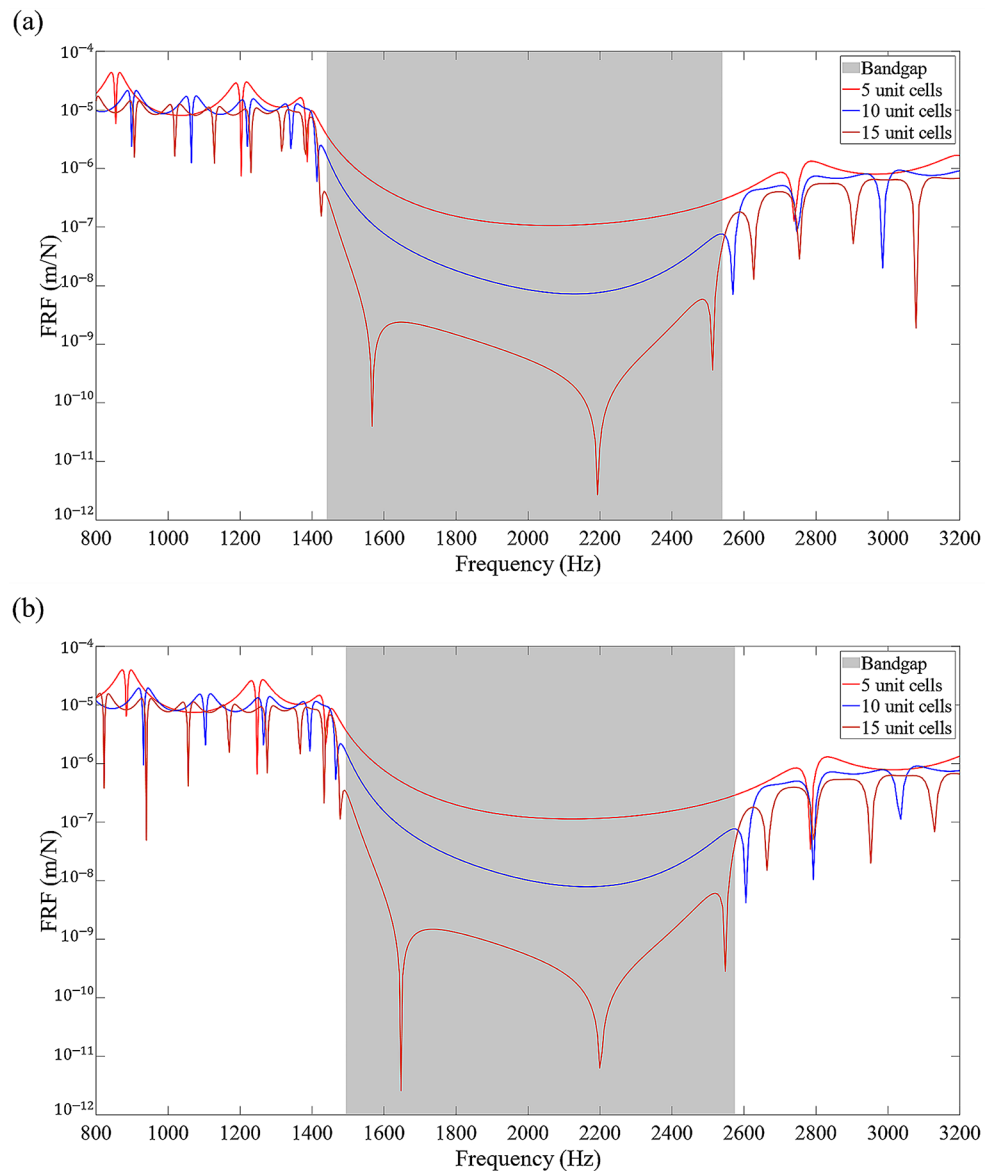


**Fig. 7** Frequency response function for different numbers of unit cells for (a) Scheme A and (b) Scheme B



number of unit cells, the proposed schemes A and B with different numbers of unit cells (5, 10, and 15 unit cells) are performed in this section. Figure 8 depicts the FRFs obtained with different numbers of unit cells for schemes A and B. The shaded frequency ranges in Fig. 8 correspond to the bandgaps obtained from the results displayed in Fig. 2. The low transmissibility of the flexural wave is consistent with the predicted bandgap, and the bandgap behavior is notable for both proposed structures. The level of vibration amplitude significantly decreases within the bandgap when the number of unit cells is increased to 15, which agrees well with the observation in the literature [1, 16]. This phenomenon occurs because as a wave travels through unit cells, it interacts with reflected waves, which reduces its amplitude within the bandgap frequency. Consequently, the amplitude of the wave decreases as it passes through each unit cell, and the amplitude loss is amplified as the wave propagates through the sandwich beam.

Figure 8 displays the displacement fields of the proposed structures with 10 unit cells at different frequencies. Figure 8(a) and (c) show the displacement fields excited at 1603 Hz and 1694 Hz for schemes A and B respectively, and both excited frequencies are located in the bandgap as discussed in Fig. 2. It can be seen that the displacements are attenuated rapidly and do not propagate to the right side of the structures. When out-of-bandgap frequencies at 2808 Hz and 2716 Hz for schemes A and B are applied to the structures, the displacements are propagated to the right side of the structures without attenuation as shown in Fig. 8(b) and (d).

## Effect of Delamination on the FRF

Delamination is the main damage events in composite sandwich structures, which usually reduces the stiffness and strength of the composites and leads to the catastrophic failure of the entire structures. Therefore, the effect of delamination on the performance of vibration attenuation is investigated in this subsection. The proposed schemes A and B with 15 unit cells are discussed to see the effect of face–core delamination on the FRF. Figure 9 illustrates the delamination area in red, where exists in the middle between the top surface of the core and the bottom surface of the upper CFRP face sheet. Surface-to-surface contact without tie constraints is defined in the delamination area of the FE model. The delamination lengths, which is 20% and 60% of the total structural lengths, investigated in this study. Figure 10(a) and (b) presents an FRF comparison of a pristine conventional composite sandwich with those of pristine/delaminated proposed schemes A and B, respectively. It can be seen that the pristine conventional composite sandwich (black solid line) has no attenuation of displacement compared to the proposed structures. The performances of vibration attenuation for both pristine proposed structures (red solid line) are better than the delaminated structures (dash line). As the delamination length increased, the performance of vibration attenuation worsens within the bandgap (grey area) and the bandgap behavior could not be clearly observed. Nevertheless, the delaminated structures for both schemes still exhibit better performance of vibration attenuation than the pristine conventional composite sandwich.

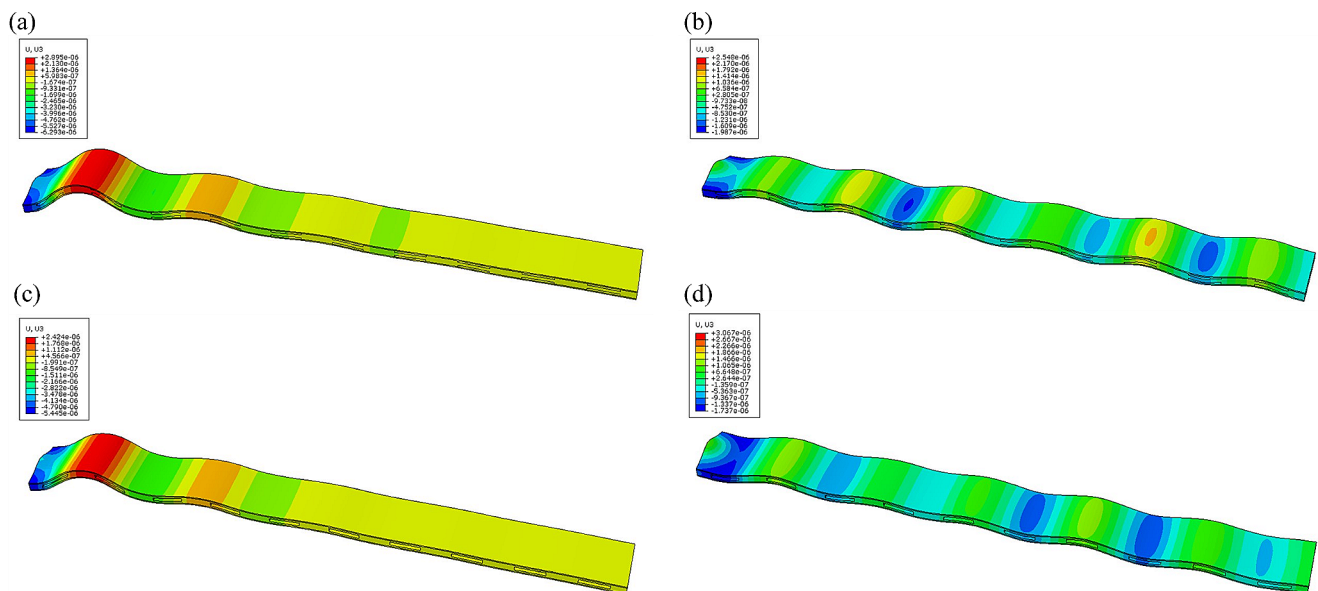


**Fig. 8** Displacement response of the proposed structures. Scheme A excitation at (a) 1603 Hz (within bandgap) and (b) 2808 Hz (out of bandgap). Scheme B excitation at (c) 1694 Hz (within bandgap) and (d) 2716 Hz (out of bandgap)

**Fig. 9** Schematics of the face–core delamination for the proposed structures with 15 unit cells

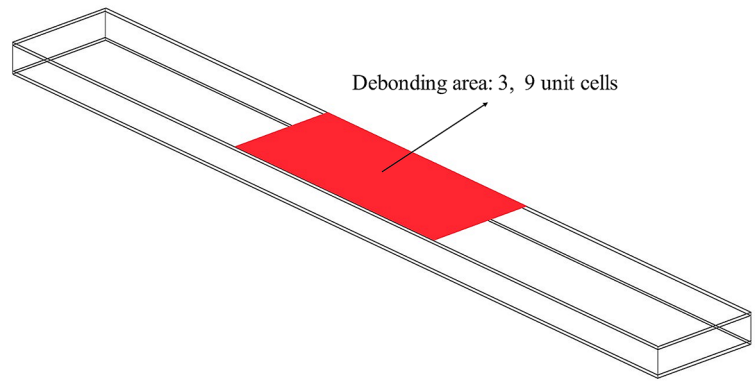
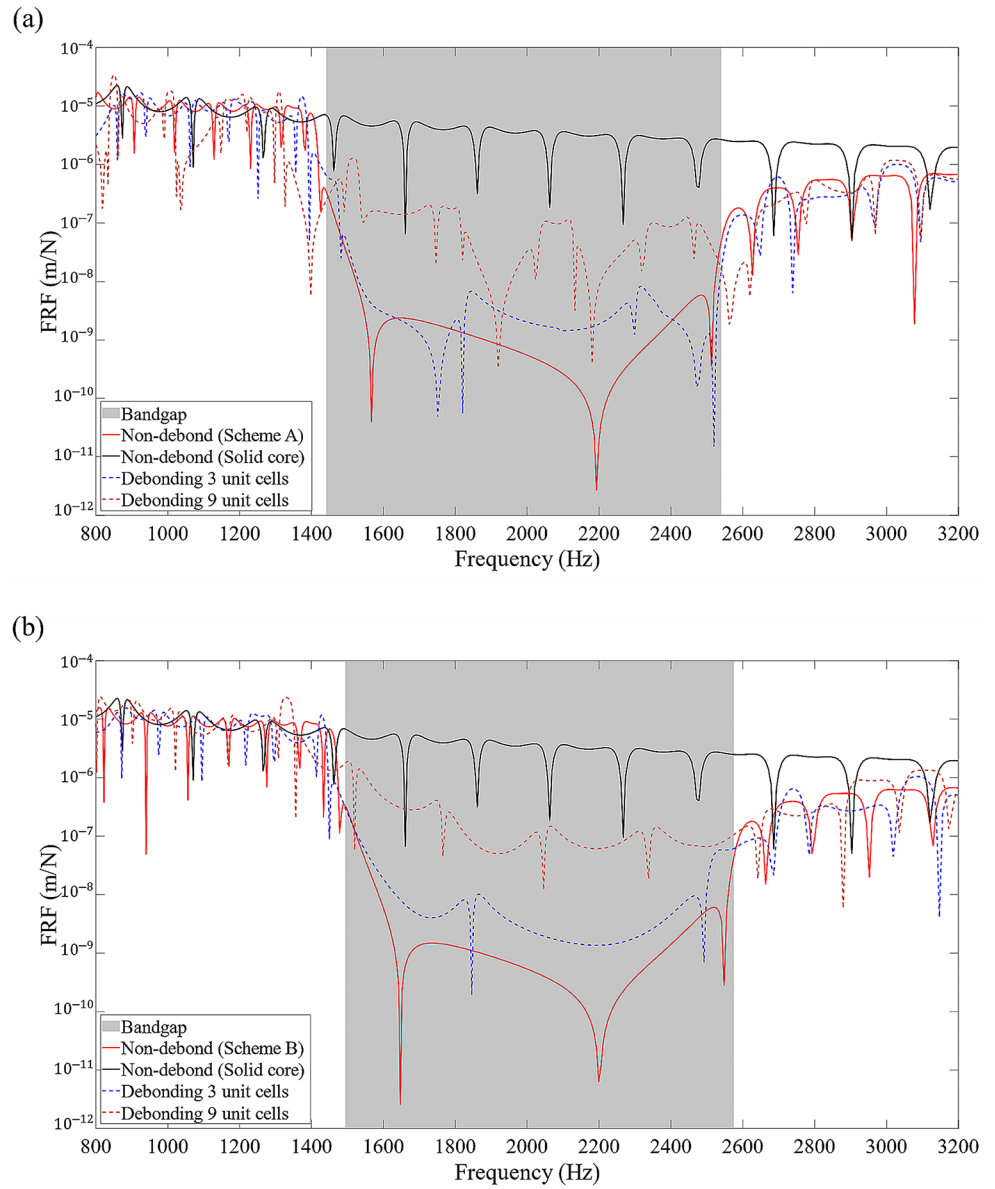


**Fig. 10** Frequency response function of pristine (red solid line) and delaminated (dash line) proposed structures compared with the conventional composite sandwich with solid core (black solid line) for (a) Scheme A and (b) Scheme B



## Conclusion

In this paper, two lightweight types of composite sandwich structures with periodic hollow-shaped cores are proposed to have a wide flexural bandgap in intermediate-to-low-frequency ranges. First, parametric studies are conducted to investigate the influence of core geometric dimensions to the flexural bandgap. Changing the core width is more effective in reducing the bandgap frequency whereas increasing the core thickness leads to a larger RBW. In most cases, the RBW of scheme A is slightly larger than that of scheme B. Next, the FRF simulations are performed to investigate the performance of vibration attenuation for the proposed structures, and the simulated results agree well with the predicted bandgap. When the number of unit cells is increased, the displacement amplitude decreases considerably. Last, the effect of delamination on the FRF are examined. The simulated results indicate that the performance of vibration attenuation is getting worse as the delamination length increased. Nevertheless, the delaminated proposed structures still have better performance of vibration attenuation than the pristine conventional sandwich structures. Our findings demonstrate that despite the simplicity of the core design, it is capable of achieving comparable bandgap behavior to more complex geometries.

**Supplementary Information** The online version contains supplementary material available at <https://doi.org/10.1007/s42417-024-01420-1>.

**Acknowledgements** This work is supported by National Science and Technology Council (NSTC) in Taiwan through the grant MOST 111-2222-E-006 -009 -MY2.

## Declarations

**Conflict of interest** The authors declare that they have no conflict of interest.

## References

1. Ampatzidis T, Leach RK, Tuck CJ, Chronopoulos D (2018) Band gap behaviour of optimal one-dimensional composite structures with an additive manufactured stiffener, *Compos B Eng*, vol. 153, pp. 26–35, Nov. <https://doi.org/10.1016/j.compositesb.2018.07.012>
2. Valiya Valappil S, Aragón AM, Goosen H (Feb. 2023) Phononic crystals' band gap manipulation via displacement modes. *Solid State Commun* 361:115061. <https://doi.org/10.1016/j.ssc.2022.115061>
3. Chen Z, Wang G, Shi F, Lim CW (Jun. 2022) Analytical modeling and numerical analysis for tunable topological phase transition of flexural waves in active sandwiched phononic beam systems. *Int J Mech Sci* 223:107292. <https://doi.org/10.1016/j.ijmecsci.2022.107292>
4. Cheng Y, Liu XJ, Wu DJ (2011) Band structures of phononic-crystal plates in the form of a sandwich-layered structure, *J Acoust Soc Am*, vol. 130, no. 5, pp. 2738–2745, Nov. <https://doi.org/10.1121/1.3641365>
5. Guo Z, Sheng M, Pan J (Jul. 2017) Flexural wave attenuation in a sandwich beam with viscoelastic periodic cores. *J Sound Vib* 400:227–247. <https://doi.org/10.1016/j.jsv.2017.04.016>
6. Hussein MI, Hulbert GM, Scott RA (2006) Dispersive elastodynamics of 1D banded materials and structures: analysis, *J Sound Vib*, vol. 289, no. 4–5, pp. 779–806, Feb. <https://doi.org/10.1016/j.jsv.2005.02.030>
7. Hussein MI, Leamy MJ, Ruzzene M (2014) Dynamics of Phononic Materials and Structures: Historical Origins, Recent Progress, and Future Outlook, *Appl Mech Rev*, vol. 66, no. 4, Jul. <https://doi.org/10.1115/1.4026911>
8. Pelat A, Gallot T, Gautier F (Apr. 2019) On the control of the first Bragg band gap in periodic continuously corrugated beam for flexural vibration. *J Sound Vib* 446:249–262. <https://doi.org/10.1016/j.jsv.2019.01.029>
9. Yu K, Chen T, Wang X (May 2013) Band gaps in the low-frequency range based on the two-dimensional phononic crystal plates composed of rubber matrix with periodic steel stubs. *Phys B Condens Matter* 416:12–16. <https://doi.org/10.1016/j.physb.2013.02.011>
10. Zhang Z, Han XK, Ji GM (2018) Mechanism for controlling the band gap and the flat band in three-component phononic crystals, *Journal of Physics and Chemistry of Solids*, vol. 123, pp. 235–241, Dec. <https://doi.org/10.1016/j.jpcs.2018.08.012>
11. Moscatelli M, Ardito R, Driemeier L, Comi C (Aug. 2019) Band-gap structure in two- and three-dimensional cellular locally resonant materials. *J Sound Vib* 454:73–84. <https://doi.org/10.1016/j.jsv.2019.04.027>
12. Mizukami K, Kawaguchi T, Ogi K, Koga Y (Jan. 2021) Three-dimensional printing of locally resonant carbon-fiber composite metastructures for attenuation of broadband vibration. *Compos Struct* 255:112949. <https://doi.org/10.1016/j.compstruct.2020.112949>
13. Ding L, Ding B, Wu Q-Y, Zhu H-P (2023) Flexural Wave Propagation in a Double-Beam System Interconnected by Local Resonators with Two Degrees of Freedom, *J Eng Mech*, vol. 149, no. 2, Feb. <https://doi.org/10.1061/JENMDT.EMENG-6762>
14. An X, Yuan X, Hou X, Fan H (Feb. 2023) Low frequency vibration attenuation of meta-orthogrid sandwich panel with high load-bearing capacity. *Compos Struct* 305:116560. <https://doi.org/10.1016/j.compstruct.2022.116560>
15. Chen JS, Sharma B, Sun CT (2011) Dynamic behaviour of sandwich structure containing spring-mass resonators, *Compos Struct*, vol. 93, no. 8, pp. 2120–2125, Jul. <https://doi.org/10.1016/j.compstruct.2011.02.007>
16. Domadiya PG, Manconi E, Vanali M, Andersen LV, Ricci A (2016) Numerical and experimental investigation of stop-bands in finite and infinite periodic one-dimensional structures, *Journal of Vibration and Control*, vol. 22, no. 4, pp. 920–931, Mar. <https://doi.org/10.1177/1077546314537863>
17. Park S, Jeon W (May 2021) Ultra-wide low-frequency band gap in a tapered phononic beam. *J Sound Vib* 499:115977. <https://doi.org/10.1016/j.jsv.2021.115977>
18. Acar G, Yilmaz C (2013) Experimental and numerical evidence for the existence of wide and deep phononic gaps induced by inertial amplification in two-dimensional solid structures, *J Sound Vib*, vol. 332, no. 24, pp. 6389–6404, Nov. <https://doi.org/10.1016/j.jsv.2013.06.022>
19. Yuksel O, Yilmaz C (Oct. 2015) Shape optimization of phononic band gap structures incorporating inertial amplification mechanisms. *J Sound Vib* 355:232–245. <https://doi.org/10.1016/j.jsv.2015.06.016>

20. Liang Y-J, Dávila CG, Iarve EV (Nov. 2021) A reduced-input cohesive zone model with regularized extended finite element method for fatigue analysis of laminated composites in Abaqus. *Compos Struct* 275:114494. <https://doi.org/10.1016/j.compstruct.2021.114494>
21. Liang Y-J, McQuien JS, Iarve EV (May 2020) Implementation of the regularized extended finite element method in Abaqus framework for fracture modeling in laminated composites. *Eng Fract Mech* 230:106989. <https://doi.org/10.1016/j.engfracmech.2020.106989>
22. Wu K-J, Young W-B (Aug. 2022) Internal characteristics analysis of woven/unidirectional composite angle part by VBO process. *Compos Commun* 33:101215. <https://doi.org/10.1016/j.coco.2022.101215>
23. Wu K-J, Young W-B (2023) Complex angle part fabricated by vacuum bag only process with interleaved dry fiber and prepreg, *J Compos Mater*, vol. 57, no. 2, pp. 199–211, Jan. <https://doi.org/10.1177/00219983221143229>
24. Karsandik Y, Sabuncuoglu B, Yildirim B, Silberschmidt VV (Jun. 2023) Impact behavior of sandwich composites for aviation applications: a review. *Compos Struct* 314:116941. <https://doi.org/10.1016/j.compstruct.2023.116941>
25. Ampatzidis T, Chronopoulos D (Aug. 2019) Mid-frequency band gap performance of sandwich composites with unconventional core geometries. *Compos Struct* 222:110914. <https://doi.org/10.1016/j.compstruct.2019.110914>
26. Kim H-Y, Hwang W (Jan. 2002) Effect of debonding on natural frequencies and frequency response functions of honeycomb sandwich beams. *Compos Struct* 55(1):51–62. [https://doi.org/10.1016/S0263-8223\(01\)00136-2](https://doi.org/10.1016/S0263-8223(01)00136-2)
27. Tsai S-N, Taylor AC (Feb. 2019) Vibration behaviours of single/multi-debonded composite sandwich structures with nanoparticle-modified matrices. *Compos Struct* 210:590–598. <https://doi.org/10.1016/j.compstruct.2018.11.071>
28. Mead DJ (1973) A general theory of harmonic wave propagation in linear periodic systems with multiple coupling, *J Sound Vib*, vol. 27, no. 2, pp. 235–260, Mar. [https://doi.org/10.1016/0022-460X\(73\)90064-3](https://doi.org/10.1016/0022-460X(73)90064-3)
29. Phani AS, Woodhouse J, Fleck NA (2006) Wave propagation in two-dimensional periodic lattices, *J Acoust Soc Am*, vol. 119, no. 4, pp. 1995–2005, Apr. <https://doi.org/10.1121/1.2179748>
30. Mace BR, Manconi E (2008) Modelling wave propagation in two-dimensional structures using finite element analysis, *J Sound Vib*, vol. 318, no. 4–5, pp. 884–902, Dec. <https://doi.org/10.1016/j.jsv.2008.04.039>
31. Zhao P, Zhang K, Deng Z (Sep. 2021) Size effects on the band gap of flexural wave propagation in one-dimensional periodic microbeams. *Compos Struct* 271:114162. <https://doi.org/10.1016/j.compstruct.2021.114162>
32. Liu L, Hussein MI (Jan. 2012) Wave Motion in Periodic Flexural beams and characterization of the transition between Bragg Scattering and local resonance. *J Appl Mech* 79(1). <https://doi.org/10.1115/1.4004592>
33. Jensen JS (Oct. 2003) Phononic band gaps and vibrations in one- and two-dimensional mass-spring structures. *J Sound Vib* 266(5):1053–1078. [https://doi.org/10.1016/S0022-460X\(02\)01629-2](https://doi.org/10.1016/S0022-460X(02)01629-2)

**Publisher's Note** Springer Nature remains neutral with regard to jurisdictional claims in published maps and institutional affiliations.

Springer Nature or its licensor (e.g. a society or other partner) holds exclusive rights to this article under a publishing agreement with the author(s) or other rightsholder(s); author self-archiving of the accepted manuscript version of this article is solely governed by the terms of such publishing agreement and applicable law.